Received: 8 October 2023 | Revised: 21 November 2023 | Accepted: 1 December 2023

DOI: 10.1002/agt2.475

Aggregate Open Access WILEY

RESEARCH ARTICLE

Thermally activated delayed fluorescence Au-Ag-oxo nanoclusters: From photoluminescence to radioluminescence

Peng Yuan[1,2,†] | **Hansong Zhang**[1,†] | **Yang Zhou**[3,†] | **Tengyue He**[3,†] | **Sami Malola**[4] | **Luis Gutiérrez-Arzaluz**[3] | **Yingwei Li**[5] | **Guocheng Deng**[1] | **Chunwei Dong**[2] | **Renwu Huang**[2] | **Xin Song**[2] | **Boon K. Teo**[1] | **Omar F. Mohammed**[3] | **Hannu Häkkinen**[4] | **Osman. M. Bakr**[2] | **Nanfeng Zheng**[1,6,‡]

[1]New Cornerstone Science Laboratory, State Key Laboratory for Physical Chemistry of Solid Surfaces, Collaborative Innovation Center of Chemistry for Energy Materials, National and Local Joint Engineering Research Center of Preparation Technology of Nanomaterials, College of Chemistry and Chemical Engineering, Xiamen University, Xiamen, China

[2]KAUST Catalysis Center (KCC), Division of Physical Sciences and Engineering, King Abdullah University of Science and Technology (KAUST), Thuwal, Saudi Arabia

[3]Advanced Membranes and Porous Materials Center, Division of Physical Science and Engineering, King Abdullah University of Science and Technology (KAUST), Thuwal, Saudi Arabia

[4]Department of Physics and Chemistry, Nanoscience Center, University of Jyväskylä, Jyväskylä, Finland

[5]Department of Chemistry and Chemical Biology, Harvard University, Cambridge, Massachusetts, USA

[6]Innovation Laboratory for Sciences and Technologies of Energy Materials of Fujian Province (IKKEM), Xiamen, China

Correspondence
Nanfeng Zheng and Peng Yuan, New Cornerstone Science Laboratory, State Key Laboratory for Physical Chemistry of Solid Surfaces, Collaborative Innovation Center of Chemistry for Energy Materials, National and Local Joint Engineering Research Center of Preparation Technology of Nanomaterials, College of Chemistry and Chemical Engineering, Xiamen University, Xiamen, China.
Email: nfzheng@xmu.edu.cn; peng.yuan@kaust.edu.sa

Osman M. Bakr, KAUST Catalysis Center (KCC), Division of Physical Sciences and Engineering, King Abdullah University of Science and Technology (KAUST), Thuwal, Saudi Arabia.
Email: osman.bakr@kaust.edu.sa

Hannu Häkkinen, Department of Physics and Chemistry, Nanoscience Center, University of Jyväskylä, Jyväskylä, Finland.
Email: hannu.j.hakkinen@jyu.fi

[‡]This author is a lead contact.

Funding information
National Natural Science Foundation of China, Grant/Award Numbers: 92261207, 21890752; NSFC Center for Single-Atom Catalysis, Grant/Award Number: 22388102; New Cornerstone Science Foundation; King Abdullah University of Science and Technology; Academy of Finland, Grant/Award Numbers: 292352, 319208

Abstract

Thermally activated delayed fluorescence (TADF) materials have numerous applications in energy conversion and luminescent imaging. However, they are typically achieved as metal-organic complexes or pure organic molecules. Herein, we report the largest Au-Ag-oxo nanoclusters to date, $Au_{18}Ag_{26}(R_1COO)_{12}(R_2C{\equiv}C)_{24}(\mu_4\text{-}O)_2(\mu_3\text{-}O)_2$ (**$Au_{18}Ag_{26}$**, where R_1 = CH_3-, Ph-, CHOPh- or CF_3Ph-; R_2 = Ph- or FPh-). These nanoclusters exhibit exceptional TADF properties, including a small S_1-T_1 energy gap of 55.5 meV, a high absolute photoluminescence quantum yield of 86.7%, and a microseconds TADF decay time of 1.6 μs at ambient temperature. Meanwhile, **$Au_{18}Ag_{26}$** shows outstanding stability against oxygen quenching and ambient conditions. Atomic level analysis reveals the strong $\pi\cdots\pi$ and C-H$\cdots\pi$ interactions from the aromatic alkynyl ligands and the enhancement of metal-oxygen-metal interactions by centrally coordinated O^{2-}. Modeling of the electronic structure shows spatially separated highest occupied molecular orbital and lowest unoccupied molecular orbital, which promote charge transfer from the ligand shell, predominantly carboxylate ligands, to O^{2-}-embedded metal core. Furthermore, TADF Au-Ag-oxo nanoclusters exhibit promising radioluminescence properties, which we demonstrate for X-ray imaging. Our work paves the way for the design of TADF materials based on large metal nanoclusters for light-emission and radioluminescence applications.

KEYWORDS
Au-Ag-oxo nanoclusters, photoluminescence, radioluminescence, TADF, X-ray imaging

[†]Peng Yuan, Hansong Zhang, Yang Zhou, Tengyue He contributed equally to this work.

1 | INTRODUCTION

Thermally activated delayed fluorescence (TADF) materials have gained much attention and have been extensively utilized in organic light-emitting diodes, X-ray scintillation, and biological imaging.[1–6] Compared with traditional fluorescent and phosphorescent materials, TADF materials can remarkably achieve 100% internal quantum efficiency through a reverse intersystem crossing (RISC) process from the lowest triplet excited state (T_1) to the lowest singlet excited state (S_1).[5,7] The singlet excitons generated from absorbed triplet excitons can emit in an efficient fluorescence process, which will promote the efficient utilization of triplet excitons. Generally, the highly efficient TADF materials require spatial separation of the highest occupied molecular orbital (HOMO) and the lowest unoccupied molecular orbital (LUMO) which can result in a very small energy gap (ΔE_{ST}) between S_1 and T_1 to promote RISC process. Currently, TADF materials are predominantly reported on mononuclear, oligonuclear metal-organic complexes and pure organic molecules with several microseconds to several milliseconds photoluminescent lifetimes.[8,9] Additionally, most of them exhibit diminished TADF behavior in the presence of O_2 due to O_2 has a strong quenching effect on triplet state emission.[10,11] There is an urgent need for novel TADF materials with excellent ambient stability for the development of multifunctional applications.

In the last decade, atomically precise photoluminescent metal nanoclusters have been the emerging link between luminescent organometallic complexes and traditional metal nanoclusters.[12–14] Understanding the origin of photoluminescence (PL) at the atomic level has been helping to create highly luminescent nanomaterials for specific applications.[15–18] In the early stage, researchers mainly focused on the particle size effects and valence states of metal atoms.[19–21] The intraband transitions of the free electrons in the M(0) core were well-accepted as an important origin of PL of metal nanoclusters.[22,23] More recently, with the fast development of atomically precise ligand-capped metal nanoclusters,[12,13,14,24–28] the understanding of the luminescence mechanism shifted to the roles played by cluster aggregation,[29–31] surface ligands,[32–35] kernel atoms,[36–41] and (ligand shell)-(metal core) interactions.[42–44] Inspired by these insights on the origin of PL, an increasing number of metal nanoclusters (e.g., Ag_6 95%,[45] $C@Au_6Ag_6$ 92%,[46,47] $Au@Cu_{14}$ 71%,[38] and Ag_{64} 97%[48]) possess quantum yields (QYs) that are competitive with those exhibited by quantum dots such as CdS[38,45,46,47] but are often achieved as low-nuclearity. It should be noted that those reported highly luminescent nanoclusters usually have several microseconds lifetimes, but only a few show TADF properties.[45,49–51] The synthesis of highly efficient TADF nanoclusters sheds light on the process of understanding the mechanism of luminescence and the applications of nanoscale PL particles in photoelectric applications.

In this work, we report the facile synthesis and detailed structural characterization of a new series of TADF Au-Ag-oxo nanoclusters protected by alkynyl and carboxylate ligands with absolute QYs as high as 86.7%. The general formula of the nanoclusters is $Au_{18}Ag_{26}(R_1COO)_{12}(R_2C{\equiv}C)_{24}(\mu_4\text{-}O)_2(\mu_3\text{-}O)_2$ (abbreviated hereafter as $\mathbf{Au_{18}Ag_{26}}$, where R_1, R_2 = CH_3, Ph (**1a**); CH_3, FPh (**1b**); Ph, Ph (**2a**); Ph, FPh (**2b**); CHOPh, Ph (**3a**); CHOPh, FPh (**3b**); CF_3Ph, Ph (**4**). In addition, the enhanced room-temperature PL and a small energy separation between the singlet S_1 and triplet T_1 state of $\Delta E(S_1{-}T_1)$ = 447 cm^{-1} (55 meV) are characterized as TADF properties. Density functional theory (DFT) analysis provided further insights into the electronic structure of these clusters and implied (i) a strong charge redistribution between the Au-Ag-oxo core and ligand shell and (ii) different spatial localization of filled and empty electron orbitals around the HOMO-LUMO energy gap as likely factors contributing to the long-lifetime ultra-bright luminescence. Taking advantage of the high atomic weight content of the $\mathbf{Au_{18}Ag_{26}}$ nanoclusters and their efficient TADF behavior, we demonstrate their X-ray-to-visible light converting capabilities and promising X-ray scintillation imaging performance.

2 | RESULTS AND DISCUSSION

2.1 | Synthesis and structure analysis of Au-Ag-oxo nanoclusters

In general, R_1COOAg, $R_2C{\equiv}CAg$ and Ag_2O were firstly added to the turbid solution of $R_2C{\equiv}CAu$ under vigorous stirring. A clear orange red solution was then obtained by centrifugation and orange red rhombic crystals (Figure S1A) were formed in one day. We have successfully synthesized 7 Au-Ag-oxo nanoclusters with different R_1 and R_2 substituents (Figures S2–S8, S10, and S11 and Table S8-11). Herein, we take $Au_{18}Ag_{26}(CHOPhCOO)_{12}(PhC{\equiv}C)_{24}(\mu_4\text{-}O)_2(\mu_3\text{-}O)_2$ ($\mathbf{Au_{18}Ag_{26}}$**-3a**) as the model to illustrate the atomically precise structure of the Au-Ag-oxo nanoclusters. The $\mathbf{Au_{18}Ag_{26}}$**-3a** nanoclusters crystallized in space group $P2_1/n$ (Figure S9). $\mathbf{Au_{18}Ag_{26}}$**-3a** has a van der Waals diameter of about 2.2 nm (including the ligand shell) with a metal core diameter of about 1.4 nm, which is consistent with the particle-size distribution from transmission electron microscopy (TEM) images (Figure S1B).

Within the Au-Ag-oxo metal core of $\mathbf{Au_{18}Ag_{26}}$**-3a**, the 18 Au atoms constitute three helical stripes with a crystallographic inversion center (Figure S12), whereas the 26 Ag atoms are wrapping outside (Figure 1A). The metal framework can also be regarded as an $Au_{12}O_4@Au_6Ag_{26}$ core-shell structure (Figure 1B and Figure S13). The 12 Au atoms in the central core are arranged in four layers of Au_3 equilateral triangles possessing C_3 symmetry, with each Au_3 plane having an interstitial oxide ion (O^{2-}) at the center (on the C_3 symmetry axis) (Figure 1B, Figures S8b and S14). For the planes of interior Au_3 equilateral triangles, O^{2-} coordinate with 3 Au atoms (μ_3-O, Figure 1D); for the planes of exterior Au_3 equilateral triangles, O^{2-} not only coordinate with 3 Au atoms, but also coordinate with the Ag atoms on the threefold axis (idealized or crystallographic, vide infra) to form a tetrahedral coordination for the interstitial oxide ion (μ_4-O, Figure 1C). It can also be described as having a "layer-by-layer" structure derived from idealized three-layer face-centered-cubic (*fcc*) arrangements **ABC** and **C´B´A´**as depicted in Figure S15. Here the top three **ABC** layers are related to the bottom three **C´B´A´** layers by a crystallographic inversion center (Figure 1B and Figure

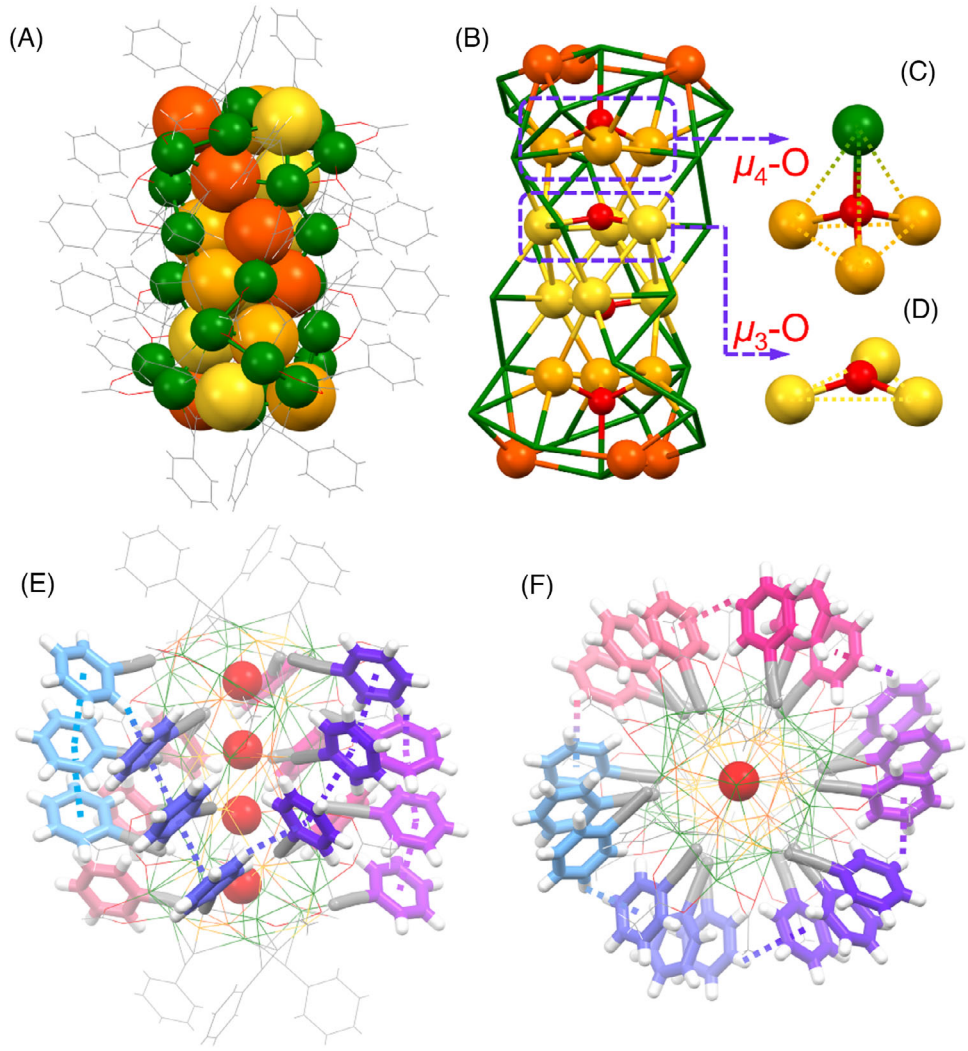

FIGURE 1 The molecular structure of **$Au_{18}Ag_{26}$-3a**. (A) The Au-Ag-oxo metal core with three Au helical stripes highlighted in large size and different colors. (B) The Au-Ag-oxo metal core with Au atoms highlighted in ABCC´B´A´ stacking. (C and D) The coordination modes of μ_4-O (C) and μ_3-O (D). Au = yellow, orange, dark orange, Ag = green, O = red, C = gray, H = white. (E and F) Side and top views of the coordination modes of surface ligands with $\pi\cdots\pi$ stacking (E) and C-H$\cdots\pi$ interactions (F). Carbons belong to different ligand sets are marked in different colors, and the μ_3-O and μ_4-O are highlighted in large size. The phenyl rings of carboxylate ligands are omitted for clarity.

S15), resulting in an overall **ABCC´B´A´** stacking. Due to the O^{2-} coordination, the distances between the Au atoms in the Au_3 surface layer are much greater than that in the bulk Au (2.884 Å), being 3.30 Å and 3.45 Å for interior and exterior Au_3 equilateral triangles (Table S1 and S2), respectively, indicating that they are weak Au-Au interactions. The average Au-O distance is 2.069 Å, suggesting strong interactions between interstitial O^{2-} and the core Au(I) atoms (four stacked Au_3 triangles).[52,53] In addition, strong interactions between the surface PhC≡C- ligands are observed in the nanocluster crystal structure. As shown in Figure 1E,F and Figures S16-S17, the adjacent phenyl rings are dominated by dislocated stacking $\pi\cdots\pi$ interactions. Six sets of interacting PhC≡C- are found in the organic shell, and each set contains three alkynyl ligands (Figure 1E,F, marked in different colors) with the center distances between adjacent phenyl rings are 3.630 and 3.653 Å, respectively. Moreover, C-H$\cdots\pi$ interactions are also observed between the two phenyl rings belonging to different sets (Figure 1E,F), resulting in a giant interacting organic shell covering the Au-Ag-oxo core. The strong intracluster interactions effectively increase the rigidity of the organic shell and thus, reduce the nonradiative energy loss, which could be related to the strong PL of the title nanoclusters.

2.2 | TADF properties of Au-Ag-oxo nanoclusters

Single crystals of Au-Ag nanoclusters were dissolved in $CHCl_3$ and the ultraviolet–visible (UV-vis) absorption spectra were measured (Figure S18), showing a weak absorption peak in the range of 300–550 nm. The resulting solution exhibited bright orange-yellow fluorescence under 365 nm irradiation (Figure S19) with intense emission behavior at 596–612 nm (Figure S20A and Table S3), indicating that the Au-Ag-oxo nanoclusters have a large Stokes shift (ST) (Figures S21 and S22, Table S3). In addition, the photoluminescent decay curves of these Au-Ag-oxo nanoclusters were fitted by a bi-exponential decays, which including a short (τ_1) and a long (τ_2) component. As shown in Table S4, the contribution of τ_2 component to the average lifetime (τ_{av}) is significantly greater than that of the τ_1 component. The achieved average lifetime of those Au-Ag-oxo nanoclusters reach the

level of μs, specifically 1.57–1.98 μs (Figure S20B and Table S3). The large ST and the μs-level of PL lifetime indicate that the emission may be related to triplet excitation.[47,54,55] In addition, the absolute QYs of the nanoclusters in solution were measured under 365-nm excitation, and unexpectedly reached a maximum of 86.7% at room temperature (RT). At present, there are many studies on the fluorescence emission behavior of metal nanoclusters, but most of them focused on the low-nuclearity (<25), and there are few examples with QYs of greater than 80%.[45,46,47] We believe that, in our system, the strong $\pi\cdots\pi$ interactions (Figure 1E, F, and Figure S16) among the well-parallel-stacked phenyl groups of the surface ligands greatly restricts the motion of the surface ligands, resulting in the observed strong fluorescence. More importantly, the PL of **$Au_{18}Ag_{26}$-3a** shows negligible attenuation in the presence of O_2, confirming stability against oxygen quenching and ambient conditions (Figure S23). The singlet oxygen ($^1O_2$) generation experiments also demonstrated that the photoexcited **$Au_{18}Ag_{26}$** cannot effectively transfer energy/charge to oxygen to generate $^1O_2$ (Figure S24).[38,48,56] The quenching of PL in **$Au_{18}Ag_{26}$-3a** is nearly imperceptible primarily due to the fact that the rate of quenching by O_2 is significantly slower, with a $k_q[O_2]_{air}$ value of approximately 1.6×10^3 s^{-1} ($[O_2]_{air}$ = 1.71 mM for $CHCl_3$), which is much smaller than the intrinsic PL decay rate, τ_{N2}^{-1}, estimated to be around 4.4×10^5 s^{-1} (Figure S23B).[56]

To gain a deeper understanding of the photophysical properties of **$Au_{18}Ag_{26}$** nanoclusters, temperature-dependent PL measurements were performed on **$Au_{18}Ag_{26}$-3a**-PMMA film over a range of 80 to 340 K (Figure 2A,C, Figures S25 and S26). The results showed that the emission energy of **$Au_{18}Ag_{26}$-3a** increased as the temperature increased from 80 to 340 K, leading to a blue shift in the maximum emission from 616 nm (80 K) to 601 nm (340 K) upon excitation at 365 nm (Figure 2C and Figure S26). Additionally, as the temperature rose from 80 to 92 K, the intensity of the emission peaks initially decreased before increasing again as the temperature further rose to 340 K (Figure 2D). At low temperatures (80–92 K), the relaxation processes could be inhibited, leading to a lower population of emissive singlet states with slower rate of RISC (k_{RISC}). However, as the temperature increases beyond this range (>92 K), the thermal energy becomes sufficient to activate these relaxation processes, which can overcome the energy barrier between T_1 and S_1 states, increasing the RISC rate. This activation energy facilitates the conversion of triplets to singlets, resulting in a higher population of emissive states. Furthermore, the decay times at various temperatures were successfully measured and plotted versus temperature (Figure 2E,F and Figure S27), which shows nearly a plateau at temperatures below 110 K. At such low temperatures, the population is predominantly frozen in the T_1 state, a constant value of 5.40 μs was observed, representing the phosphorescence decay time (τ) for the $T_1 \rightarrow S_0$ transition. Above 110 K, the decay time progressively shortened as the temperature increased due to the thermal population of the higher-lying S_1 state, resulting in a τ (300 K) value of 1.64 μs (Figure 2B). The temperature-dependent photoluminescence decay curves exhibited bi-exponential decays, characterized by a short component (τ_1) and a long component (τ_2). Table S5 shows that the contribution of τ_2 to the average lifetime (τ_{av}) is notably higher than that of τ_1. It also appears that the τ_1 component barely changes with increasing temperature and has a lifetime range of 15–35 ns, but the τ_2 component gradually decreases with increasing temperature from 5.36 to 1.4 μs. Fitting the temperature-dependent PL decay lifetimes of **$Au_{18}Ag_{26}$-3a** to the modified Boltzmann equation (please see the details about equation 1 in the supporting information) gave an activation energy of $\Delta E(S_1\text{-}T_1)$ = 0.0555 eV and a radiative rate of fluorescence of $k^r(S_1\text{-}S_0) = 1.08 \times 10^7$ s^{-1}. The radiative rate of phosphorescence ($k^r(T_1\text{-}S_0)$) was found to be 1.87×10^5 s^{-1}, corresponding to a phosphorescence decay time of $\tau(T_1\text{-}S_0)$ = 5.4 μs. This observation is similar to other TADF materials, where RISC from the T_1 state to the S_1 state leads to delayed fluorescence.[2,3,5,8,9,49] At temperatures below 110 K, only long-lasting phosphorescence is observed as the T_1 to S_0 transition has a decay time of 5.4 μs. As the temperature increases, rapid internal conversion (IC) results in a population of the S_1 state with a higher energy than the T_1 state. This results in a 15 nm blue-shift of the emission from Au-Ag-oxo nanoclusters with TADF, which is consistent with the activation energy of 447 cm^{-1} for the S_1 to T_1 transition, as determined from the analysis of the decay times. The S_1 to S_0 transition rate of TADF material is much higher compared to other organo-metallic TADF materials.[2,3,5,8,9,49] As a result, the TADF decay time at 300 K is significantly reduced to 1.64 μs, which benefits from the small $\Delta E(S_1\text{-}T_1)$ and the large $k^r(S_1\text{-}S_0)$ (Figure 2B). Few TADF metal nanoclusters have been reported, and most of them display low QYs and long lifetimes in solution.[45,49,50,51] Compared to these TADF nanoclusters (Table S6), our $Au_{18}Ag_{26}$ nanoclusters display the largest nuclearity, the highest QY and the shortest TADF lifetime in solution.

We investigated the ultrafast electron dynamics of the **$Au_{18}Ag_{26}$-3a**-PMMA film using femtosecond and nanosecond transient absorption (TA) measurements to gain a deeper understanding of the excited-state process on the early time scale. As seen in Figure 2G, two excited state absorptions (ESAs) were observed at 550 and 700 nm after photoexcitation at 400 nm, which begin to decay after a time delay of 0.5 ps. The wide range of ESA band at 450–750 nm indicates that **$Au_{18}Ag_{26}$-3a** has dense excited states. The kinetic traces for these bands, shown in Figures S28 and S29A, exhibit a sub-ps decay of 756 fs and 557 fs for 550 and 700 nm, respectively, which can be attributed to IC and vibrational relaxation (VR) to the S_1 state.[57,58] The second time component, 808 and 1006 ps, is due to the combination of delayed VR process and radiative decay at semi-relaxed state (Figure S28).[57] The longer remaining components were determined using ns-TA, as shown in Figure 2H,I and Figure S29, two distinct unimolecular decay mechanisms were identified to match TADF: the prompt fluorescence (PF) and the delayed fluorescence (DF). The delayed component has a decay time of 1.13 ± 0.10 μs and 1.14 ± 0.23 μs for 550 and 700 nm, respectively. The prompt component has a decay time of 33.13 ± 3.2 ns and 43.11 ± 2.0 ns and can be assigned to the fluorescence of **$Au_{18}Ag_{26}$**, which is consistent with the short component (τ_1: 15–35 ns) obtained for the excited-state decay lifetime. The key photophysical rates can be determined using the experimental prompt and delayed emission lifetimes and the photoluminescence quantum efficiency of **$Au_{18}Ag_{26}$-3a**-PMMA film, yielding $k_{ISC} = 1.95 \times 10^7$ s^{-1}

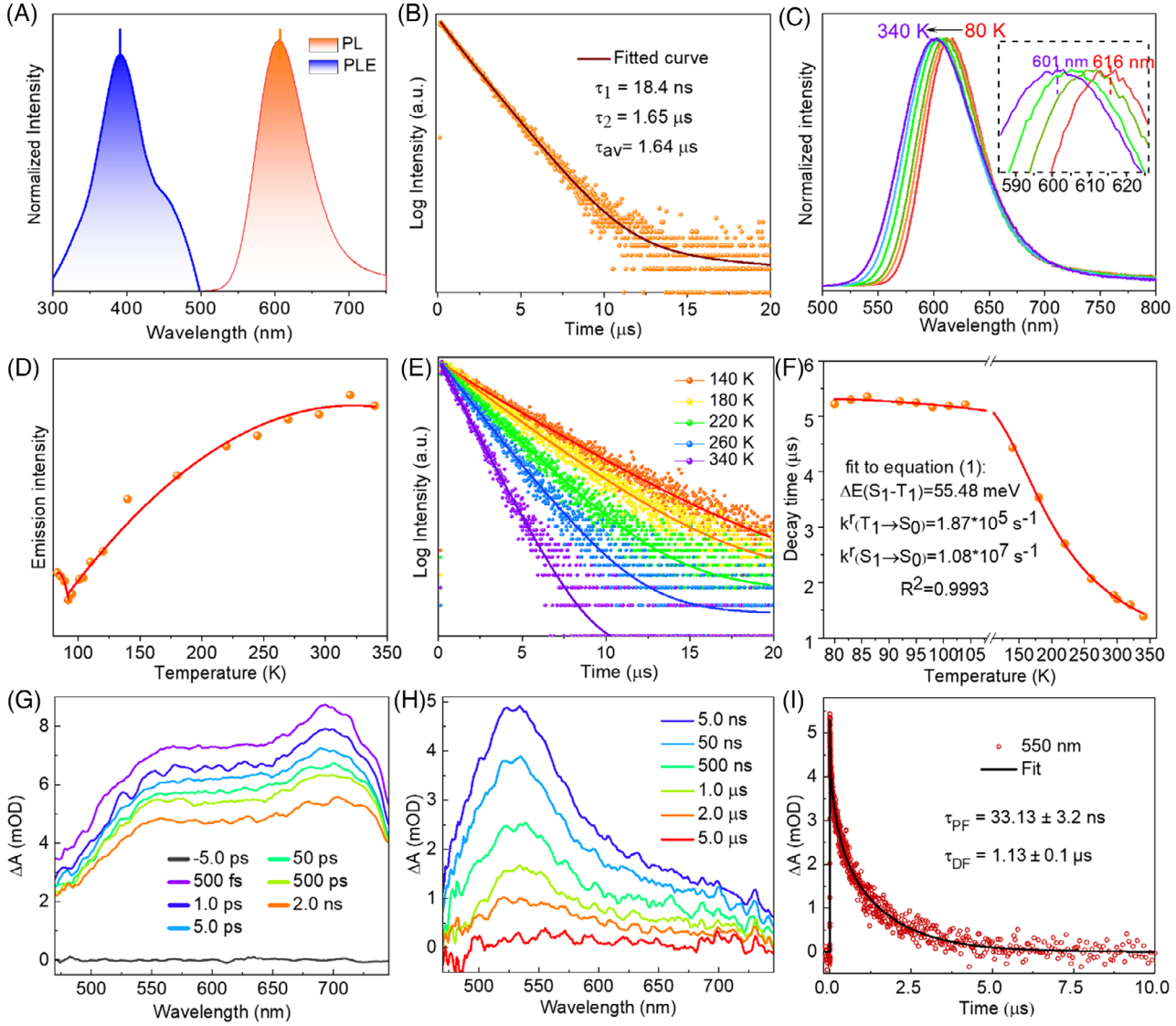

FIGURE 2 Emission and transient absorption spectra of $\mathbf{Au_{18}Ag_{26}}$**-3a** in PMMA film. (A) Normalized emission and excitation spectra. (B) Excited-state lifetime decay at 300 K. (C) Normalized temperature-dependent emission in the range of 80 to 340 K. (D and E) Temperature-dependent emission intensity (D) and excited-state lifetimes (E) in the range of 80 to 340 K. (F) Temperature dependence of the in the range of 80 to 340 K. Plot of emission decay lifetime against temperature (80 to 340 K); the red line represents the fit according to the thermally activated delayed fluorescence (TADF) equation (see Equation (1) in the supporting information). (G and H) Time evolution of transient absorption spectra 0.5 ps-2 ns (G) and 5 ns-5 μs (H) after excitation at 400 nm. (I) Kinetic trace probed at 550-nm wavelength in μs-scale time window.

and $k_{RISC} = 9.43 \times 10^5\ s^{-1}$, which are consistent with other TADF molecules.[2,3,5,8,9,49] According to the emission QYs and the decay times, one can figure out the radiative decay rate $k^r = \Phi_{PL}/\tau$ (300 K) $= 3.75 \times 10^5\ s^{-1}$, suggesting that RT emission contains contributions of delayed fluorescence and phosphorescence,[9] which can also be reflected by a continuous increase in emissive energy from 300 to 350 K. The high radiative TADF decay rate leads to an emission quantum yield of 60% at ambient temperature. The ratio of $I(S_1)/I(T_1) \approx 2.25$ at ambient temperature suggests that the emission spectrum is dominated by 70% TADF and 30% phosphorescence from T_1.[9] The correspondence between the activation energy and the spectral shift upon temperature increase further supports the assignment of the ambient temperature emission as TADF, although it is noted that the emission at ambient temperature may not only represent TADF but also contain some $T_1 \rightarrow S_0$ (phosphorescence) contribution (Figure S30).

2.3 | Radioluminescence of Au-Ag-oxo nanoclusters

In addition to PL properties, many highly TADF materials usually exhibit excellent radioluminescence (RL) properties.[4,59,60] Owing to the small triplet–singlet energy separation, TADF materials significantly facilitates luminescent harvesting of radiation-induced triplet excitons,[4,59,60] which can be developed as radiation scintillators to convert high-energy radiation (X-rays and gamma rays) into visible light photons. Nonetheless, research on radioluminescence properties of metal nanoclusters remain relatively scarce.[60–62] Metal nanoclusters are very attractive for the design of X-ray responsive materials and have great potential in X-ray imaging.[63,64] On the one hand, metal nanoclusters have a high atomic number (Z) and good luminescence efficiency, resulting a considerable X-ray absorption capacity.[63,65] On the other hand, metal nanoclusters are

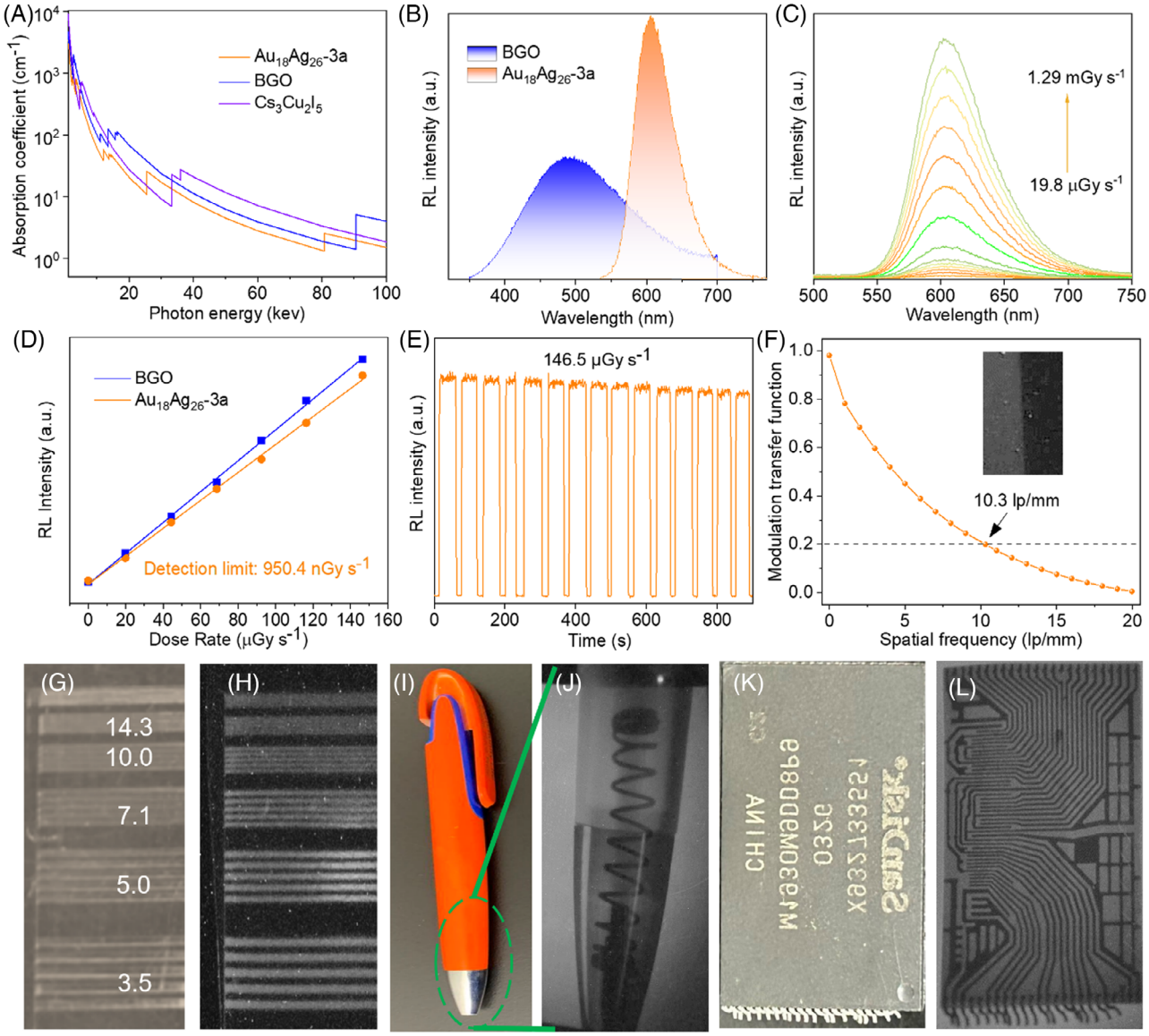

FIGURE 3 The radioluminescence properties of **$Au_{18}Ag_{26}$-3a** nanocluster. (A) X-ray absorption spectra of **$Au_{18}Ag_{26}$-3a**, $Bi_4Ge_3O_{12}$ (BGO), and $Cs_3Cu_2I_5$ measured as a function of the irradiation energy. (B) RL spectra of **$Au_{18}Ag_{26}$-3a** and BGO at the optimal thickness (dose rate, 146.5 μGy s^{-1}). (C) Dose rate-dependent RL spectra of **$Au_{18}Ag_{26}$-3a** over the dose rate range of 19.8 μGy s^{-1} to 1.29 mGy s^{-1}. (D) Detection limits of $Au_{18}Ag_{26}$-3a and BGO. (E) The RL stability of **$Au_{18}Ag_{26}$-3a** under continuous X-ray irradiation (dose rate, 146.5 μGy s^{-1}). (F) Modulation transfer function (MTF) of the **$Au_{18}Ag_{26}$-3a**-PMMA film, measured by the slanted-edge method (inset). (G and H) The optical (G) and X-ray photographs (H) of a standard X-ray resolution pattern plate (lp/mm). (I and J) Photographs of a ball pen with a metal spring inside before (I) and after (J) X-ray exposure. (K and L) Photographs of an electronic chip before (K) and after (L) X-ray exposure.

low-temperature solution-processable and highly soluble, which can be incorporated into organic polymers for preparing high flexibility and high transparency hybrid films.[63,66] Pay more attention in the metal nanoclusters scintillator may open a new world for the application of TADF metal nanoclusters. To study the radioluminescence performance of **$Au_{18}Ag_{26}$-3a**, the X-ray absorption capability was first determined, which is comparable to that of $Bi_4Ge_3O_{12}$ (BGO) and $Cs_3Cu_2I_5$ scintillators (Figure 3A). Under X-ray excitation, **$Au_{18}Ag_{26}$-3a** shows a radioluminescence spectra peaked at 600 nm, which is the same as the photoluminescence spectra under UV excitation (Figure S31). The integrated RL intensity of **$Au_{18}Ag_{26}$-3a** corresponds to the standard scintillation (BGO), which has a light yield of 10,000 photons MeV^{-1} (Figure 3B). Also, the RL intensities of **$Au_{18}Ag_{26}$-3a** exhibited an excellent linear response at higher dose rates from 19.8 μGy s^{-1} to 1.29 mGy s^{-1} (Figure 3C), resulting in a low X-ray dose rates of 950.4 nGy s^{-1} (Figure 3D). Moreover, the X-ray radiation stability was further evaluated (Figure 3E). The RL intensity of TADF **$Au_{18}Ag_{26}$-3a** nanoclusters remained >93% under ionizing radiation (146.5 μGy s^{-1}) continuously applied for 900 s (Figure 3E), which showed the excellent radiation resistance of **$Au_{18}Ag_{26}$-3a** nanoclusters. In addition, the intensity of the UV-vis spectra does not decrease significantly between 300 and 500 nm, which demonstrates the stability of the nanoclusters under continuous X-ray irradiation (Figure S32). A uniform large-area (4 × 4 cm^2) **$Au_{18}Ag_{26}$-3a**-PMMA film with a thickness of ~40 μm was prepared to further investigate the potential applications in X-ray imaging (Figures S33-S35). The light transmittance in the visible light range is up to 80% (Figure S33), indicating that the **$Au_{18}Ag_{26}$-3a**-PMMA film possesses negligible light scattering effect. It is noteworthy that the poor optical transparency caused by light scattering usually results

in reduced X-ray imaging spatial resolution.[67] Moreover, the X-ray image of standard line chart shows a high spatial resolution with distinguishable line space of ~10 lp mm^{-1}, which was further demonstrated by the modulation transfer function using slanted-edge method (Figure 3F–H and Figure S36). Such a high spatial resolution is even comparable to that of commercial CsI (Tl) scintillator.[65,67] In addition, a ball pen with a metal spring inside and an electronic chip were used as imaging objects, as shown in Figure 3I–L, the outline of the inside metal spring and inner structure could be clearly presented on the film through the plastic case. We attribute the high spatial resolution to the homogeneous distribution and large Stokes shift of **$Au_{18}Ag_{26}$-3a** nanoclusters that mitigates the light scattering effect and self-absorption behavior of emitted X-ray.

2.4 | Mechanism of luminescent properties of Au-Ag-oxo nanoclusters

It is generally believed that PL intensity of M(I) nanoclusters appears to be stronger than M(0)/M(I) nanoclusters.[45,46,47,68] This special charge balance system is bound to affect the photoluminescence properties of the material, particularly Au-Ag-oxo metal nanoclusters usually accompanied by excellent luminescence.[51,54,69] The addition of negatively charged atoms, such as C^{4-}, N^{3-}, P^{3-}, O^{2-} and S^{2-}, helps to enhance the aggregation of Au and Ag, forming the unique regioselective distribution of two different metal ions and changing the physical and chemical properties of the resulting nanocluster.[52,53,70] In addition, the above studies have shown that the $\pi\cdots\pi$ interactions between surface ligands can drive the different crystallization behaviors of nanocluster molecules and affect the rigidity of the surface ligands, thereby enhancing the fluorescence properties of metal nanoclusters.[32]

DFT calculations performed directly on the crystal structure of the **$Au_{18}Ag_{26}$** nanocluster confirm significant charge transfer inside the nanocluster (Table S7). The accumulated positive Bader charge for the metal atoms is 17.5 |e|, compensated partially by the total negative charge of −3.6 |e| of the oxo-species. In the ligand shell, the 24 PhC≡C and 12 CH_3COO ligands have total charges of −6.0 |e| and −7.9 |e|, respectively. The HOMO-LUMO energy gap is significant, 1.76 eV, confirming the stability of the nanocluster. The computed UV-vis absorption spectrum is in a qualitative agreement with the measured one and shows an optical gap at about 705 nm corresponding exactly to the HOMO-LUMO gap (Figure S37). This implies that the lowest optical transitions involve the frontier orbitals around the gap as shown by the dipole transition contribution map analysis close to the optical band edge (Figure S38). We analyzed the electronic density of states around the HOMO-LUMO energy gap by decomposing it to atom/ligand types (Figure 4A–D) and formed the combined spatial density from a few orbitals closest to the gap (Figure 4D). The orbitals just below the gap have weight on metal atoms, acetate ligands, and to a minor extent on the PA-metal interface. On the other hand, acetate ligands do not contribute to the density just above the gap. As with conventional organic TADF materials, the Au-Ag-oxo metal core acts as an acceptor and the surface ligand (especially acetate ligands) acts as a donor. This creates an interesting spatial redistribution of the charge in the hypothetical LUMO-HOMO transition, if the main mechanism for the emitted photon in the luminescence involves the orbitals around the gap. Hence, the spatially separating HOMO and LUMO orbitals greatly promoted the ligand-to-metal charge transfer, resulting in small ΔE_{ST} values between S_1 and T_1.[71] The optimized S_1 and T_1 states (electrons being excited from HOMO to LUMO) are also visualized in Figure S39, exhibiting a qualitative similarity to the trends discussed for the frontier of the ground state calculation. In both S_1 and T_1 states, hole states are slightly more localized to the ligands and outer layers of the nanocluster than the electron states. Consequently, high emission would occur through electron transfer from the electron state back to the hole state, consistently indicating a redistribution of the charge. Furthermore, DFT calculations confirmed that the coordination of R_1COO^- is crucial for the construction and emission properties of **$Au_{18}Ag_{26}$**, which is the same as $[(C)(AuPPhpy_2)_6Ag_6(CF_3COO)_3]^{5+}$ nanocluster.[47] For traditional non-TADF metal nanoclusters, the PL intensity increased with increasing charge donating capability of ligands. But for **$Au_{18}Ag_{26}$** nanoclusters, the QYs are closely related to the strength of the electron-withdrawing group R_1-(CF_3Ph- → CHOPh- → Ph- → CH_3-) in acetate ligands, resulting 75.5% and 85.6% for CH_3- and CF_3Ph- respectively (Table S3). It is interesting to note that the phenyl rings of PA ligands do not contribute to this process. **$Au_{18}Ag_{26}$** can display excellent TADF properties, which are benefit from a small overlap of HOMO and LUMO. For CF_3Ph-functionalized Au-Ag-oxo nanoclusters, the introduction of CF_3Ph- groups contributes to the formation of π-extended donors, which can reduce the HOMO−LUMO overlap to achieve comparable energy levels for S_1 and T_1, resulting in small ΔE_{ST} values and high QYs. Overall, partial modification with CF_3Ph- groups at the appropriate position of the donor moiety can improve the luminescence efficiency of TADF nanoclusters.

In the ultraviolet absorption and conversion process, the PL of **$Au_{18}Ag_{26}$** may be attributed to ligand-to-metal charge transfer (LMCT) and/or ligand-to-metal-metal charge transfer (LMMCT), which induces radiative relaxation through a metal-centered triplet.[24,47] When the nanoclusters are excited by UV light, the electrons are excited from the ground state to the LMCT and/or LMMCT state due to the charge separation between the surface ligands and the metal atoms. The excited electrons undergo multiple processes including rapid IC, VR, intersystem crossing (ISC), and RISC, and then decay to the emitting state, characterized by the recombination of electrons and holes in the metal atom. This recombination leads to the emission of a photon characterized by our TADF Au-Ag-oxo metal nanoclusters.[15,47,57,58] Figure 4E schematically illustrates the proposed X-ray-irradiated luminescence, which differs from the photoluminescence. During the X-ray absorption and conversion process, X-ray photons directly interact with heavy atoms (Au and Ag) in the Au-Ag-oxo nanoclusters through the photoelectric effect and Compton scattering, resulting in the ejection of high-energy electrons. These hot electrons then interact with atoms in the material, leading to a cascade of secondary electrons through energy loss. This process continues to ionize or excite other molecules. After losing sufficient energy, electrons are finally captured by ligands to form hole-electron pairs. The excited

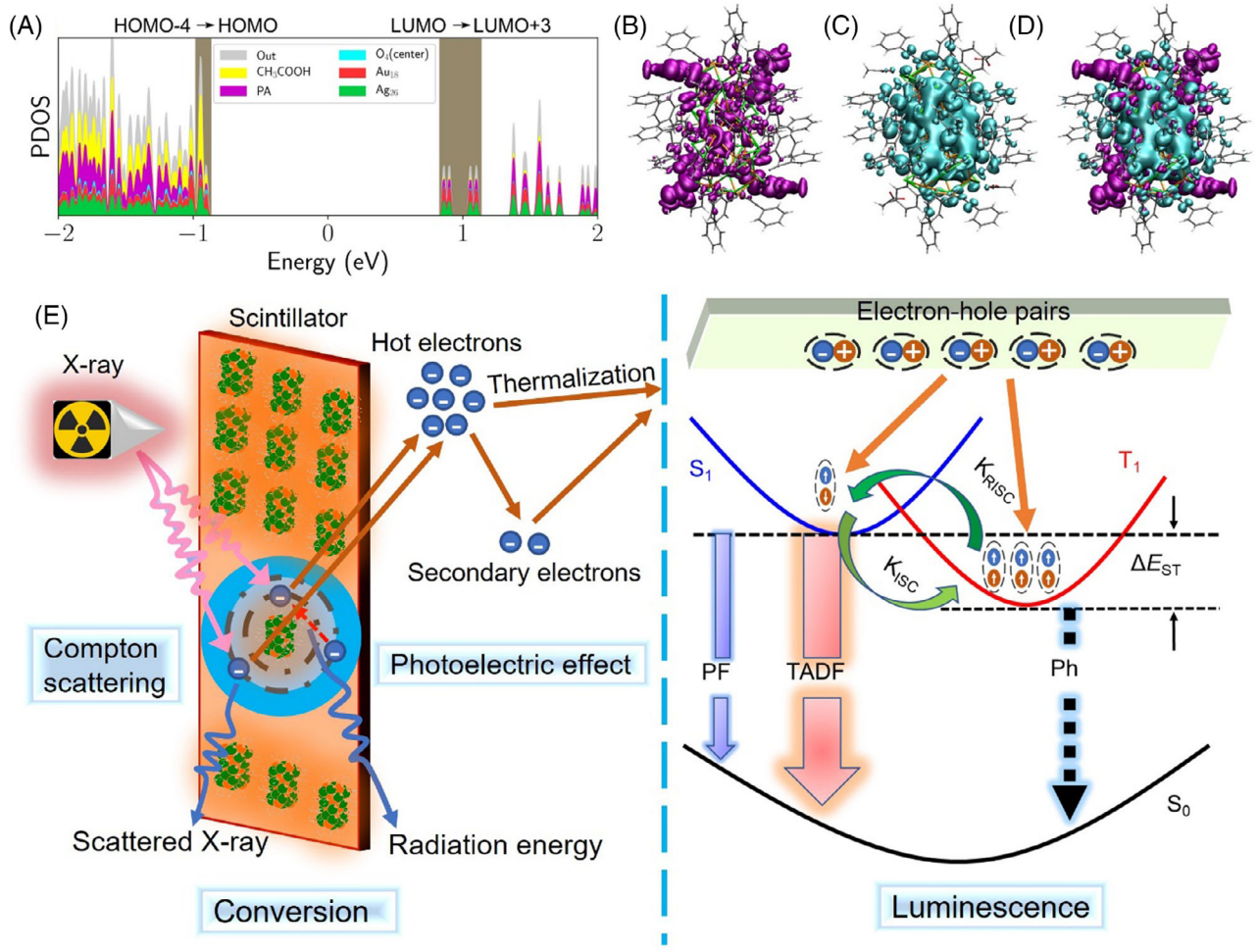

FIGURE 4 Density functional theory (DFT) and proposed mechanism of luminescence (A) Electronic density of states of $\mathbf{Au_{18}Ag_{26}}$**-1a**, decomposed into the atom/ligand types. The center of the HOMO-LUMO energy gap is at zero. (B, C, and D) Localization of electron density from the frontier orbitals around the HOMO-LUMO gap of $\mathbf{Au_{18}Ag_{26}}$**-1a** (the brown highlight in Figure 4A). Five highest occupied orbitals HOMO-4 to HOMO (B); four lowest unoccupied orbitals LUMO to LUMO+3 (C); combined density (B) + (C) (D). (E) Proposed mechanism of radioluminescence of TADF Au-Ag-oxo nanoclusters.

nanoclusters characteristic of MLCT emit RL.[4,59,61,62] Subsequently, the charge recombination between the electrons and holes produces ~25% singlet excitons and ~75% triplet excitons. Owing to the small ΔE_{ST} between S_1 and T_1 of $\mathbf{Au_{18}Ag_{26}}$, the triplet excitons can efficiently transfer to singlet excitons through a RISC process, which can result in emitting an efficient fluorescence process with a higher internal quantum efficiency.

3 | CONCLUSION

In this work, we obtained a series of TADF Au-Ag-oxo nanoclusters, showing a maximum absolute quantum yield up to 86%. The atomically precise molecular formula of the largest Au-Ag-oxo nanoclusters is $Au_{18}Ag_{26}(R_1COO)_{12}(R_2C{\equiv}C)_{24}(\mu_4\text{-}O)_2(\mu_3\text{-}O)_2$, and the core is $Au_{12}O_4$ layered structure with four interstitial O^{2-}. These TADF nanoclusters showed enhanced room-temperature PL and a small $\Delta E(S_1{-}T_1)$ value of 447 cm^{-1} (55 meV). With the help of DFT and structural analysis, the excellent luminescent properties were shown to originate from the ultrastrong $\pi\cdots\pi$ interactions by surface organic ligand, metal aggregation by the interstitial O^{2-}, strong intracluster charge transfer, and spatial differences in the localization of single-electron states around the HOMO-LUMO energy gap. In addition, the flexible and uniform $\mathbf{Au_{18}Ag_{26}}$−PMMA film was achieved, which show notable X-ray-to-visible light conversion capabilities and promise for X-ray imaging. Our work will motivate further development of TADF materials based on large nanoclusters, enabling future design and tailoring of such functional materials for X-ray imaging applications.

4 | EXPERIMENTAL SECTION

Reagents. Silver acetate (CH_3COOAg, purity 99%) was purchased from Alfa Aesar. Terephthalaldehydic acid (purity 98%), benzoic acid (purity 98%), 4-(Trifluoromethyl) benzoic acid (purity 98%), phenylacetylene (purity 98%), 1-Ethynyl-4-fluorobenzene (purity 98%), methyl sulfide (purity 99%), gold(III) chloride hydrate (purity 99.9%) were purchased from Energy Chemical Reagent Co. Ltd. (Shanghai, China). Silver nitrate ($AgNO_3$, purity 99%), triethylamine ($C_6H_{15}N$, analytical grade), and chloroform ($CHCl_3$, analytical grade) were purchased from Sinopharm Chemical Reagent Co. Ltd. (Shanghai, China). All reagents used in the experiments were used as received without further purification.

Synthesis of $Au_{18}Ag_{26}(R_1COO)_{12}(R_2C{\equiv}C)_{24}(\mu_4\text{-}O)_2(\mu_3\text{-}O)_2$. $AuSMe_2Cl$ and $R_2C{\equiv}CH$ were firstly dissolved in a solvent mixture of chloroform to obtain the $R_2C{\equiv}CAu$ precursors. Subsequently, 4 mg of CH_3COOAg, 2 mg $PhC{\equiv}CAg$ and 2 mg Ag_2O were added to the turbid solution of $PhC{\equiv}CAu$ (6 mg) under vigorous stirring. The reaction was aged for 1 h at room temperature. The solution was centrifuged for 2 min at 10000 r/min to give a clear orange red solution. Orange red block crystals were grown from $CHCl_3/C_2H_5OC_2H_5$ in 1 d after being stored at 25°C. Yield: ~50% (based on Au). To obtain single crystals with good quality of the other nanocluster, it was similar to that of $Au_{18}Ag_{26}(CH_3COO)_{12}(PhC{\equiv}C)_{24}(\mu_4\text{-}O)_2(\mu_3\text{-}O)_2$ except $R_2C{\equiv}CAu$, $R_2C{\equiv}CAg$ and R_1COOAg were used instead.

Single-Crystal Analysis. The diffraction data of $Au_{18}Ag_{26}(R_1COO)_{12}(R_2C{\equiv}C)_{24}(\mu_4\text{-}O)_2(\mu_3\text{-}O)_2$ nanoclusters were collected by an X-ray single-crystal diffractometer with Mo Kα radiation (λ = 0.710 73 Å) or Cu Kα radiation (λ = 1.54184 Å) at 100 K on an Agilent Technologies SuperNova system. The data were processed using CrysAlisPro. All crystal structures were solved and refined using fullmatrix least-squares based on F2 with the programs ShelXT and ShelXL within Olex2. More detailed refinement data are provided in Tables S8–S11. CCDC 2119531–2119537 contains the supplementary crystallographic data for this paper. These data can be obtained free of charge from The Cambridge Crystallographic Data Centre via www.ccdc.cam.ac.uk/data_request/cif.

ACKNOWLEDGMENTS

The authors acknowledge the National Natural Science Foundation of China (grant numbers: 92261207 and 21890752) and NSFC Center for Single-Atom Catalysis (grant number: 22388102), the New Cornerstone Science Foundation, the 111 Project (grant number: B08027) and the King Abdullah University of Science and Technology (KAUST) for financial support. The computational work at the University of Jyväskylä was supported by the Academy of Finland (grant numbers: 292352 and 319208). Dr. Shengchao Huang from IKKEM is acknowledged for his technical assistance in the photoluminescence measurements. Peng Yuan, Hansong Zhang, Yang Zhou, and Tengyue He contributed equally to this work.

CONFLICT OF INTEREST STATEMENT

The authors declare no conflict of interests.

ORCID

Luis Gutiérrez-Arzaluz https://orcid.org/0000-0001-8971-9377

Nanfeng Zheng https://orcid.org/0000-0001-9879-4790

REFERENCES

1. H. Uoyama, K. Goushi, K. Shizu, H. Nomura, C. Adachi, *Nature* **2012**, *492*, 234.
2. Y. Tao, K. Yuan, T. Chen, P. Xu, H. Li, R. Chen, C. Zheng, L. Zhang, W. Huang, *Adv. Mater.* **2014**, *26*, 7931.
3. X. K. Chen, D. Kim, J. L. Bredas, *Acc. Chem. Res.* **2018**, *51*, 2215.
4. J.-X. Wang, L. Gutiérrez-Arzaluz, X. Wang, T. He, Y. Zhang, M. Eddaoudi, O. M. Bakr, O. F. Mohammed, *Nat. Photon.* **2022**, *16*, 869.
5. Z. Yang, Z. Mao, Z. Xie, Y. Zhang, S. Liu, J. Zhao, J. Xu, Z. Chi, M. P. Aldred, *Chem. Soc. Rev.* **2017**, *46*, 915.
6. C. Han, Z. Zhang, D. Ding, H. Xu, *Chem* **2018**, *4*, 2154.
7. W. Yuan, H. Yang, C. Duan, X. Cao, J. Zhang, H. Xu, N. Sun, Y. Tao, W. Huang, *Chem* **2020**, *6*, 1998.
8. Z. Han, X. Y. Dong, S. Q. Zang, *Adv. Opt. Mater.* **2021**, *9*, 2100081.
9. H. Yersin, R. Czerwieniec, M. Z. Shafikov, A. F. Suleymanova, *Chemphyschem* **2017**, *18*, 3508.
10. G. Xie, X. Li, D. Chen, Z. Wang, X. Cai, D. Chen, Y. Li, K. Liu, Y. Cao, S. J. Su, *Adv. Mater.* **2016**, *28*, 181.
11. J. Liu, N. Wang, Y. Yu, Y. Yan, H. Zhang, J. Li, J. Yu, *Sci. Adv.* **2017**, *3*, e1603171.
12. I. Chakraborty, T. Pradeep, *Chem. Rev.* **2017**, *117*, 8208.
13. Y. Li, R. Jin, *J. Am. Chem. Soc.* **2020**, *142*, 13627.
14. J. Yan, B. K. Teo, N. Zheng, *Acc. Chem. Res.* **2018**, *51*, 3084.
15. H. Yu, B. Rao, W. Jiang, S. Yang, M. Zhu, *Coord. Chem. Rev.* **2019**, *378*, 595.
16. B. Li, H.-T. Fan, S.-Q. Zang, H.-Y. Li, L.-Y. Wang, *Coord. Chem. Rev.* **2018**, *377*, 307.
17. C. P. Joshi, M. S. Bootharaju, O. M. Bakr, *J. Phys. Chem. Lett.* **2015**, *6*, 3023.
18. Y. Li, Y. Song, X. Zhang, T. Liu, T. Xu, H. Wang, D. E. Jiang, R. Jin, *J. Am. Chem. Soc.* **2022**, *144*, 12381.
19. L. Gong, K. He, J. Liu, *Angew. Chem. Int. Ed.* **2021**, *60*, 5739.
20. J. Zheng, C. Zhang, R. M. Dickson, *Phys. Rev. Lett.* **2004**, *93*, 077402.
21. C. Zhou, C. Sun, M. Yu, Y. Qin, J. Wang, M. Kim, J. Zheng, *J. Phys. Chem. C Nanomater Interfaces* **2010**, *114*, 7727.
22. J. Zheng, P. R. Nicovich, R. M. Dickson, *Annu. Rev. Phys. Chem.* **2007**, *58*, 409.
23. N. Goswami, Q. Yao, Z. Luo, J. Li, T. Chen, J. Xie, *J. Phys. Chem. Lett.* **2016**, *7*, 962.
24. Z. Wu, Q. Yao, S.-q. Zang, J. Xie, *Natl. Sci. Rev.* **2020**, *8*, nwaa208.
25. P. Yuan, R. Chen, X. Zhang, F. Chen, J. Yan, C. Sun, D. Ou, J. Peng, S. Lin, Z. Tang, B. K. Teo, L. S. Zheng, N. Zheng, *Angew. Chem. Int. Ed.* **2019**, *58*, 835.
26. P. Yuan, R. Zhang, E. Selenius, P. Ruan, Y. Yao, Y. Zhou, S. Malola, H. Hakkinen, B. K. Teo, Y. Cao, N. Zheng, *Nat. Commun.* **2020**, *11*, 2229.
27. Y. Cao, S. Malola, M. F. Matus, T. Chen, Q. Yao, R. Shi, H. Häkkinen, J. Xie, *Chem* **2021**, *7*, 2227.
28. A. Ghosh, O. F. Mohammed, O. M. Bakr, *Acc. Chem. Res* **2018**, *51*, 3094.
29. X. Kang, S. Wang, M. Zhu, *Chem. Sci.* **2018**, *9*, 3062.
30. R. W. Huang, Y. S. Wei, X. Y. Dong, X. H. Wu, C. X. Du, S. Q. Zang, T. C. W. Mak, *Nat. Chem.* **2017**, *9*, 689.
31. X.-H. Wu, Z. Wei, B.-J. Yan, R.-W. Huang, Y.-Y. Liu, K. Li, S.-Q. Zang, T. C. W. Mak, *CCS Chem.* **2019**, *1*, 553.
32. M. R. Narouz, S. Takano, P. A. Lummis, T. I. Levchenko, A. Nazemi, S. Kaappa, S. Malola, G. Yousefalizadeh, L. A. Calhoun, K. G. Stamplecoskie, H. Hakkinen, T. Tsukuda, C. M. Crudden, *J. Am. Chem. Soc.* **2019**, *141*, 14997.
33. X. Kang, S. X. Wang, Y. B. Song, S. Jin, G. D. Sun, H. Z. Yu, M. Z. Zhu, *Angew. Chem. Int. Ed.* **2016**, *55*, 3611.
34. Z. Wu, R. Jin, *Nano Lett*. **2010**, *10*, 2568.
35. S. Ito, S. Takano, T. Tsukuda, *J. Phys. Chem. Lett.* **2019**, *10*, 6892.
36. Y. Zhou, L. Liao, S. Zhuang, Y. Zhao, Z. Gan, W. Gu, J. Li, H. Deng, N. Xia, Z. Wu, *Angew. Chem. Int. Ed.* **2021**, *60*, 8668.
37. M. Zhou, H. Qian, M. Y. Sfeir, K. Nobusada, R. Jin, *Nanoscale* **2016**, *8*, 7163.
38. Y. Song, Y. Li, M. Zhou, X. Liu, H. Li, H. Wang, Y. Shen, M. Zhu, R. Jin, *Sci. Adv.* **2021**, *7*, eabd2091.
39. S. Zhuang, L. Liao, J. Yuan, N. Xia, Y. Zhao, C. Wang, Z. Gan, N. Yan, L. He, J. Li, H. Deng, Z. Guan, J. Yang, Z. Wu, *Angew. Chem. Int. Ed.* **2019**, *58*, 4510.
40. Y. Wang, H. Su, L. Ren, S. Malola, S. Lin, B. K. Teo, H. Hakkinen, N. Zheng, *Angew. Chem. Int. Ed.* **2016**, *55*, 15152.
41. G. Soldan, M. A. Aljuhani, M. S. Bootharaju, L. G. AbdulHalim, M. R. Parida, A. H. Emwas, O. F. Mohammed, O. M. Bakr, *Angew. Chem. Int. Ed.* **2016**, *55*, 5749.
42. Z. Luo, X. Yuan, Y. Yu, Q. Zhang, D. T. Leong, J. Y. Lee, J. Xie, *J. Am. Chem. Soc.* **2012**, *134*, 16662.
43. K. Pyo, V. D. Thanthirige, K. Kwak, P. Pandurangan, G. Ramakrishna, D. Lee, *J. Am. Chem. Soc.* **2015**, *137*, 8244.
44. Z. Wu, Q. Yao, O. J. H. Chai, N. Ding, W. Xu, S. Zang, J. Xie, *Angew. Chem. Int. Ed.* **2020**, *59*, 9934.
45. Z. Han, X. Y. Dong, P. Luo, S. Li, Z. Y. Wang, S. Q. Zang, T. C. W. Mak, *Sci. Adv.* **2020**, *6*, eaay0107.

46. R. Zhang, C. Zhao, X. Li, Z. Zhang, X. Ai, H. Chen, R. Cao, *Dalton Trans.* **2016**, *45*, 12772.
47. Z. Lei, X. L. Pei, Z. J. Guan, Q. M. Wang, *Angew. Chem. Int. Ed.* **2017**, *56*, 7117.
48. S. S. Zhang, S. Havenridge, C. Zhang, Z. Wang, L. Feng, Z. Y. Gao, C. M. Aikens, C. H. Tung, D. Sun, *J. Am. Chem. Soc.* **2022**, *144*, 18305.
49. Z. R. Yuan, Z. Wang, B. L. Han, C. K. Zhang, S. S. Zhang, Z. Y. Zhu, J. H. Yu, T. D. Li, Y. Z. Li, C. H. Tung, D. Sun, *Angew. Chem. Int. Ed.* **2022**, *61*, e202211628.
50. X. S. Han, X. Luan, H. F. Su, J. J. Li, S. F. Yuan, Z. Lei, Y. Pei, Q. M. Wang, *Angew. Chem. Int. Ed.* **2020**, *59*, 2309.
51. L.-M. Zhang, G. Zhou, G. Zhou, H. K. Lee, N. Zhao, O. V. Prezhdo, T. C. W. Mak, *Chem. Sci.* **2019**, *10*, 10122.
52. Z. Lei, Q.-M. Wang, *Coord. Chem. Rev.* **2019**, *378*, 382.
53. Q.-M. Wang, Y.-M. Lin, K.-G. Liu, *Acc. Chem. Res.* **2015**, *48*, 1570.
54. Q. M. Wang, Y. A. Lee, O. Crespo, J. Deaton, C. Tang, H. J. Gysling, M. C. Gimeno, C. Larraz, M. D. Villacampa, A. Laguna, R. Eisenberg, *J. Am. Chem. Soc.* **2004**, *126*, 9488.
55. A. Barbieri, G. Accorsi, N. Armaroli, *Chem. Commun.* **2008**, 2185.
56. M. Mitsui, D. Arima, A. Uchida, K. Yoshida, Y. Arai, K. Kawasaki, Y. Niihori, *J. Phys. Chem. Lett.* **2022**, *13*, 9272.
57. H. Chang, N. S. Karan, K. Shin, M. S. Bootharaju, S. Nah, S. I. Chae, W. Baek, S. Lee, J. Kim, Y. J. Son, T. Kang, G. Ko, S. H. Kwon, T. Hyeon, *J. Am. Chem. Soc.* **2021**, *143*, 326.
58. L. Luo, Z. Liu, X. Du, R. Jin, *Commun. Chem.* **2023**, *6*, 22.
59. W. Ma, Y. Su, Q. Zhang, C. Deng, L. Pasquali, W. Zhu, Y. Tian, P. Ran, Z. Chen, G. Yang, G. Liang, T. Liu, H. Zhu, P. Huang, H. Zhong, K. Wang, S. Peng, J. Xia, H. Liu, X. Liu, Y. M. Yang, *Nat. Mater.* **2022**, *21*, 210.
60. P. Yuan, T. He, Y. Zhou, J. Yin, H. Zhang, Y. Zhang, X. Yuan, C. Dong, R. Huang, W. Shao, S. Chen, X. Song, R. Zhou, N. Zheng, M. Abulikemu, M. Eddaoudi, M. Bayindir, O. F. Mohammed, O. M. Bakr, *ACS Energy Lett*. **2023**, *8*, 5088.
61. Q. Hu, C. Zhang, X. Wu, G. Liang, L. Wang, X. Niu, Z. Wang, W. D. Si, Y. Han, R. Huang, J. Xiao, D. Sun, *Angew. Chem. Int. Ed.* **2023**, *62*, e202217784.
62. W. Zhao, Y. Wang, Y. Guo, Y. D. Suh, X. Liu, *Adv. Sci.* **2022**, *10*, e2205526.
63. K. Kirakci, K. Fejfarova, J. Martincik, M. Nikl, K. Lang, *Inorg. Chem.* **2017**, *56*, 4609.
64. K. Han, J. Jin, B. Su, J. Qiao, Z. Xia, *Adv. Opt. Mater.* **2022**, *10*, 2200865.
65. Y. Zhou, X. Wang, T. He, H. Yang, C. Yang, B. Shao, L. Gutiérrez-Arzaluz, O. M. Bakr, Y. Zhang, O. F. Mohammed, *ACS Energy Lett*. **2022**, *7*, 844.
66. N. Li, Z. Xu, Y. Xiao, Y. Liu, Z. Yang, S. Liu, *Adv. Opt. Mater.* **2022**, *10*, 2102232.
67. K. Han, K. Sakhatskyi, J. Jin, Q. Zhang, M. V. Kovalenko, Z. Xia, *Adv. Mater.* **2022**, *34*, e2110420.
68. G. F. Manbeck, W. W. Brennessel, R. A. Stockland, R. Eisenberg, *J. Am. Chem. Soc.* **2010**, *132*, 12307.
69. X. L. Pei, Y. Yang, Z. Lei, S. S. Chang, Z. J. Guan, X. K. Wan, T. B. Wen, Q. M. Wang, *J. Am. Chem. Soc.* **2015**, *137*, 5520.
70. Y. Yang, T. Jia, Y. Z. Han, Z. A. Nan, S. F. Yuan, F. L. Yang, D. Sun, *Angew. Chem. Int. Ed.* **2019**, *58*, 12280.
71. R. Ansari, W. Shao, S. J. Yoon, J. Kim, J. Kieffer, *ACS Appl. Mater. Interfaces* **2021**, *13*, 28529.

SUPPORTING INFORMATION

Additional supporting information can be found online in the Supporting Information section at the end of this article.

How to cite this article: P. Yuan, H. Zhang, Y. Zhou, T. He, S. Malola, L. Gutiérrez-Arzaluz, Y. Li, G. Deng, C. Dong, R. Huang, X. Song, B. K. Teo, O. F. Mohammed, H. Häkkinen, O. M. Bakr, N. Zheng, *Aggregate* **2024**, e475.
https://doi.org/10.1002/agt2.475